The 3–4-Week MJO Prediction Skill in a GFDL Coupled Model

BAOQIANG XIANG AND MING ZHAO

NOAA/Geophysical Fluid Dynamics Laboratory, Princeton, New Jersey, and University Corporation for Atmospheric Research, Boulder, Colorado

XIANAN JIANG

Joint Institute for Regional Earth System Science and Engineering, University of California, Los Angeles, Los Angeles, California

SHIAN-JIANN LIN

NOAA/Geophysical Fluid Dynamics Laboratory, Princeton, New Jersey

TIM LI AND XIOUHUA FU

International Pacific Research Center, Department of Meteorology, University of Hawai'i at Mānoa, Honolulu, Hawaii

GABRIEL VECCHI

NOAA/Geophysical Fluid Dynamics Laboratory, Princeton, New Jersey

(Manuscript received 4 February 2015, in final form 23 March 2015)

ABSTRACT

Based on a new version of the Geophysical Fluid Dynamics Laboratory (GFDL) coupled model, the Madden–Julian oscillation (MJO) prediction skill in boreal wintertime (November–April) is evaluated by analyzing 11 years (2003–13) of hindcast experiments. The initial conditions are obtained by applying a simple nudging technique toward observations. Using the real-time multivariate MJO (RMM) index as a predictand, it is demonstrated that the MJO prediction skill can reach out to 27 days before the anomaly correlation coefficient (ACC) decreases to 0.5. The MJO forecast skill also shows relatively larger contrasts between target strong and weak cases (32 versus 7 days) than between initially strong and weak cases (29 versus 24 days). Meanwhile, a strong dependence on target phases is found, as opposed to relative skill independence from different initial phases. The MJO prediction skill is also shown to be about 29 days during the Dynamics of the MJO/Cooperative Indian Ocean Experiment on Intraseasonal Variability in Year 2011 (DYNAMO/CINDY) field campaign period. This model's potential predictability, the upper bound of prediction skill, extends out to 42 days, revealing a considerable unutilized predictability and a great potential for improving current MJO prediction.

1. Introduction

As the dominant intraseasonal mode over the tropics, the Madden–Julian oscillation (MJO; Madden and Julian 1971, 1972) exerts large impacts on global weather and climate variations [see review by Zhang (2013)]. For example, the MJO exhibits a substantial modulation of the genesis and movement of tropical cyclones (e.g., Maloney and Hartmann 2000; Mo 2000; Camargo et al. 2009; Vitart 2009; Jiang et al. 2012; Murakami et al. 2015, manuscript submitted to *J. Climate*). El Niño–Southern Oscillation (ENSO) properties, such as the onset, growth rate, and amplitude, are also found to be strongly influenced by the MJO (Kessler and Kleeman 2000; Zhang and Gottschalck 2002; Lau 2005; Kug et al. 2008). The MJO also plays a

Corresponding author address: Baoqiang Xiang, GFDL, 201 Forrestal Road, Princeton, NJ 08540.
E-mail: baoqiang.xiang@noaa.gov

DOI: 10.1175/JCLI-D-15-0102.1

© 2015 American Meteorological Society

crucial role in regulating the eastern Pacific intraseasonal oscillation (Maloney and Hartmann 2000; Rydbeck et al. 2013), the West African monsoon (Matthews 2004; Alaka and Maloney 2012), and the North Atlantic Oscillation (NAO) (Cassou 2008). Through teleconnections, the impacts of MJO can be expanded to the whole globe (e.g., Donald et al. 2006; Moon et al. 2013).

A realistic MJO simulation remains as one of the most challenging issues for current climate models. In comparison to observations, many current models fail to simulate basic characteristics of the MJO by typically showing weak amplitude, slow propagation speed (or even no propagation) and long period, small ratio between the eastward and westward propagation signal, and the absence of a spectrum peak of 30–60 days (Lin et al. 2006; Kim et al. 2009; Hung et al. 2013; Jiang et al. 2015). Recently, many efforts have been made to improve our understanding of the fundamental physics related to the MJO, in particular its evolution and propagation. It has been well accepted that the lower-tropospheric moistening prior to the arrival of the intense convection plays an essential role in its eastward propagation (Kemball-Cook and Weare 2001; Benedict and Randall 2007). However, the mechanisms responsible for the lower-tropospheric moistening ahead of convection remain inconclusive and many different processes have been proposed, including the frictional moisture convergence associated with wave dynamics (e.g., Wang and Li 1994; Hsu and Li 2012), the interaction between the shallow convection and boundary layer circulation (e.g., Li et al. 2009), stratiform heating (e.g., Fu and Wang 2009), and the moisture mode destabilized by surface flux and cloud–radiative feedbacks (e.g., Sobel and Maloney 2012). By comparing 27 models that participated in the Working Group on Numerical Experimentation (WGNE) MJO Task Force and Global Energy and Water Cycle Exchanges Project (GEWEX) Atmospheric System Study program, Jiang et al. (2015) illustrated that two factors show significant correlations with MJO performance across different models: the low-level relative humidity difference between the top 5% and the bottom 10% of rain events and the seasonal mean gross moist stability.

The effective prediction of the MJO can bridge the gap between deterministic weather forecasts and probabilistic climate forecasts to extend the predictive skill of a wide range of phenomena from the synoptic scale to a climate time scale (Waliser 2005; Brunet et al. 2010; Vitart et al. 2012). The statistical models have been suggested to have skill up to 2 weeks for MJO prediction (e.g., Lo and Hendon 2000; Jiang et al. 2008; Kang and Kim 2010). MJO prediction has also been quantitatively evaluated in several dynamical models by using the same criterion (Lin et al. 2008; Vitart and Molteni 2010; Rashid et al. 2011; Wang et al. 2014; Kim et al. 2014). For instance, the Australian Bureau of Meteorology coupled ocean–atmosphere seasonal prediction system (POAMA) showed a 21-day lead forecast skill for the MJO (Rashid et al. 2011). The National Centers for Environmental Prediction (NCEP) Climate Forecast System (CFS) was shown to have useful forecast skill out to 10–15 days in version 1 (CFSv1; Seo et al. 2010) and to possess marked improvement out to 20–21 days in version 2 (CFSv2; Wang et al. 2014; Kim et al. 2014). The European Centre for Medium-Range Weather Forecasts (ECMWF) forecast system [Variable Resolution Ensemble Prediction System (VarEPS)] also exhibits prediction skill of 23–27 days for the MJO (Vitart and Molteni 2010; Kim et al. 2014).

While the basic performance in MJO simulations has been reported in previous studies for several versions of the Geophysical Fluid Dynamics Laboratory (GFDL) coupled models (e.g., Lin et al. 2006; Benedict et al. 2013), the MJO prediction skill in these models has not been examined yet. The primary goal of this study is to explore and quantitatively assess the MJO prediction skill in a new version of GFDL coupled model with a focus on the boreal winter season (November–April) when the MJO is relatively strong.

The paper is organized as follows. Section 2 introduces the model, experiments, and the verification methodology. Section 3 describes the overall MJO prediction skill and the skill dependence on MJO amplitude and phase. The predictions for MJO amplitude and propagation are documented in section 4. Section 5 presents the MJO prediction skill during the Dynamics of the MJO/Cooperative Indian Ocean Experiment on Intraseasonal Variability in Year 2011 (DYNAMO/CINDY) period. Finally, a summary and discussion are given in section 6.

2. Model, experiments, and methodology

a. Model

In this study, we use a new version of the GFDL coupled model. This model is based on the Forecast-Oriented Low Ocean Resolution (FLOR) version of GFDL model (Vecchi et al. 2014), but with a different convection scheme that is referred to as a double-plume convection (DPC) scheme (M. Zhao et al. 2015, unpublished manuscript). We use the same resolution as FLOR. The horizontal resolution for the ocean model is about 1° and it has 50 vertical levels (10-m resolution in the upper 100 m). The atmospheric model has an

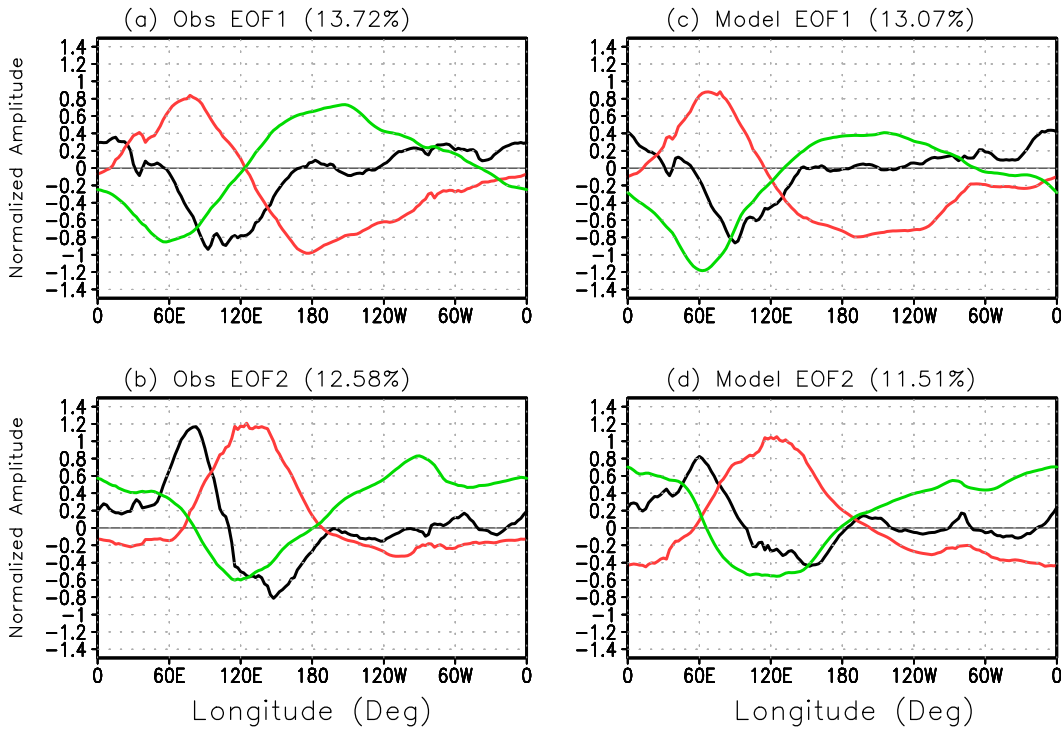

FIG. 1. The (a) first and (b) second EOF modes of combined fields of OLR (black), U850 (red), and U200 (green). Here we used the NOAA OLR data and NCEP GFS analysis wind data (2002–13). (c),(d) As in (a),(b), but for model's free coupled run (20 yr). The percentage value in parentheses above each panel is the variance explained by each mode.

approximately 50-km horizontal resolution and 32 vertical levels. This model has been used to demonstrate the beyond weather time scale prediction for specific typhoon/hurricane cases (Xiang et al. 2014).

A realistic simulation of MJO is usually regarded as a necessary (but not sufficient) condition for a skillful MJO prediction. Since it is a widely used metric for characterizing observed MJO evolution and measuring the intrinsic MJO modes, we examined the combined EOF developed by Wheeler and Hendon (2004, hereafter WH04). Figure 1 depicts the spatial structure of the combined EOF modes of the anomalous outgoing longwave radiation (OLR), 850-hPa zonal winds (U850), and 200-hPa zonal winds (U200) averaged between 15°S and 15°N. For observations, the first EOF (EOF1) mode features an enhanced convection over the eastern Indian Ocean and Maritime Continent (MC), while the second EOF (EOF2) mode displays the intensified convection over the western Pacific together with the suppressed convection over the Indian Ocean (Fig. 1). The associated circulation (U850 and U200) shows an out-of-phase pattern for the upper and lower troposphere zonal winds, representing a dynamically coherent baroclinic structure. The lead–lag correlation of these two PCs reveals the maximum correlation with EOF1 leading EOF2 for about 10 days. A fully coupled control run (20 yr) was also made to evaluate the performance of the coupled model in simulating the intrinsic MJO mode. The model generally captures the convection–circulation coupled patterns for both EOF modes as well as their explained variances (Figs. 1c,d). Compared with EOF1 mode, the EOF2 mode shows relatively larger bias in the model. For example, the maximum convection tends to occur too far eastward and U200 exhibits a broad peak without a clear maximum center (Fig. 1d). A more detailed documentation of the importance of the DPC scheme in improving MJO simulation will be provided in M. Zhao et al. (2015, unpublished manuscript).

b. *Hindcast experiments*

Initial conditions and the boundary forcing [e.g., sea surface temperature (SST)] are equally important for a skillful MJO prediction (Waliser 2006). In this study, initial conditions for atmosphere and ocean were obtained through a nudging technique toward the observations. The atmospheric nudging fields include winds, temperature, geopotential height, and surface pressure using the NCEP Global Forecast System (GFS) analysis data (6-hourly interval). The SST is nudged to the

National Oceanic and Atmospheric Administration (NOAA) optimum interpolation ¼° daily SST analysis, version 2 (OISSTv2; Reynolds et al. 2007). The nudging time scale is 6 h for atmospheric variables and 1 day for SST.

To obtain the initial conditions, we first spin up the coupled system with the observed atmospheric and SST nudging for 11 years to allow the ocean (particularly the upper ocean) to adjust. Starting from the above initial conditions, we made another round of nudging from January 2003 to December 2013 to create initial conditions for hindcast experiments. Since this study aims to explore the MJO prediction skill during boreal winter season, hindcasts were carried out every 5 days for each month from November to April. An ensemble is generated by having initial conditions from successively 4 h apart, namely, at 0000, 0400, 0800, 1200, 1600, and 2000 UTC, forming a daily six-member ensemble. In total we made 396 (11 yr × 6 months × 6 cases) forecast cases during the 11 years and each has six members so that the total number of forecast sets is 2376. For each run, we integrated the model for 50 days.

c. Methodology

Following WH04, the observational anomalous fields (OLR, U850, and U200) are obtained by applying the following two steps: 1) removing the time mean and first 3 harmonics of the climatological annual cycle from the observational data (2002–13) and 2) subtracting the 120-day mean of the previous 120 days in order to remove the influence of the interannual and even longer time-scale variability. Following Neena et al. (2014), the hindcast fields anomalies are obtained by removing the model hindcast climatology as a function of starting date of hindcast and lead day. The hindcast climatology includes the signal from both model climatology and also the initial shock and model drift. After this, we also apply step 2 above to remove the interannual variability for hindcast anomalies (appending the corresponding observed anomaly fields before the forecast).

The above observational and predicted anomalous fields are then projected on to the two observational EOF modes (Figs. 1a,b) to obtain the MJO principal component (PC) indices, also named the real-time multivariate MJO (RMM) indices (WH04). Both the observed and hindcast RMM indices are then normalized by the standard deviation of the observed RMM indices. In this study, we took the NOAA daily mean interpolated OLR data (Liebmann and Smith 1996) and NCEP GFS analysis data (including U850 and U200) as observations.

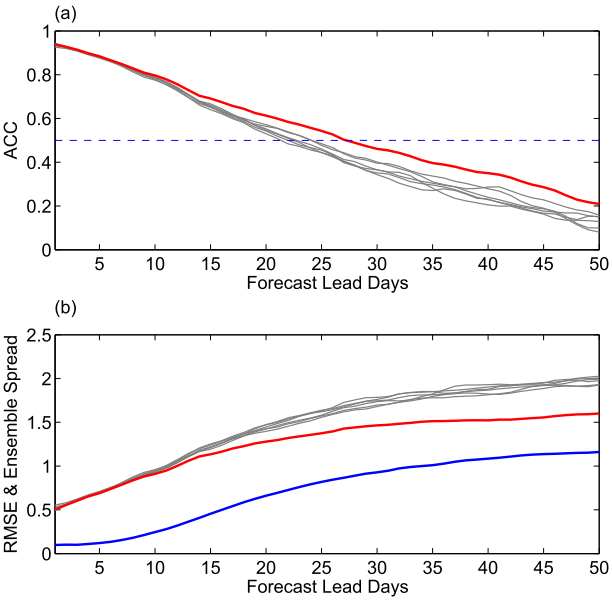

FIG. 2. MJO prediction skill in boreal winter. (a) The bivariate ACC for individual member (gray) and six-member ensemble mean (red) as a function of forecast lead days. (b) RMSE of individual member (gray) and ensemble mean (red), and the ensemble spread relative to the six-member ensemble mean (blue).

Using the above RMM indices as the predictands, the so-called bivariate anomaly correlation coefficient (ACC) and bivariate RMSE were adopted here to measure its forecast skill (Lin et al. 2008; Rashid et al. 2011):

$$\mathrm{ACC}(\tau) = \frac{\sum_{t=1}^{N} [a_1(t)b_1(t,\tau) + a_2(t)b_2(t,\tau)]}{\sqrt{\sum_{t=1}^{N} [a_1^2(t) + a_2^2(t)]}\sqrt{\sum_{t=1}^{N} [b_1^2(t,\tau) + b_2^2(t,\tau)]}}$$

and

$$\mathrm{RMSE}(\tau) = \sqrt{\frac{1}{N}\sum_{t=1}^{N} [|a_1(t) - b_1(t,\tau)|^2 + |a_2(t) - b_2(t,\tau)|^2]}.$$

Here $a_1(t)$ and $a_2(t)$ are the verification RMM1 and RMM2 at time t; $b_1(t, \tau)$ and $b_2(t, \tau)$ are the corresponding forecasts at time t for a lead time of τ days; and N is the number of forecasts. It is regarded that the skill is useful when the bivariate ACC is greater than 0.5 at which the RMSE increases to the level of prediction with climatology (Lin et al. 2008; Rashid et al. 2011; Wang et al. 2014). More details of the evaluation method can be found in Lin et al. (2008) and Rashid et al. (2011).

TABLE 1. Summary of the MJO prediction skill (days) in this version of the GFDL model.

All	Initial strong	Initial weak	Target strong	Target weak	Initial weak and target strong	DYNAMO	Predictability
27	29	24	32	7	27	29	42

To examine the propagation speed error in prediction, the phase angle error is estimated between the observed and the predicted RMM indices following Rashid et al. (2011):

$$\mathrm{ERR}_{\mathrm{phs}}(\tau) = \frac{1}{N}\sum_{t=1}^{N} \tan^{-1}\left[\frac{a_1(t)b_2(t,\tau) - a_2(t)b_1(t,\tau)}{a_1(t)b_1(t,\tau) + a_2(t)b_2(t,\tau)}\right].$$

The bivariate amplitude is defined as $[a_1^2(t) + a_2^2(t)]^{1/2}$ for observations and for $[b_1^2(t) + b_2^2(t)]^{1/2}$ model forecasts. The total observed and predicted MJO cases (396) are separated into initially strong and weak cases based on the observed MJO amplitude. An MJO is defined as a strong case when its amplitude is larger than 1.0 (246 cases; 62% of total observation cases) and a weak case for those equal to or less than 1.0 (150 cases; 38% of total observation cases) during the period of 2003–13.

3. Overall MJO prediction skill

In this section, emphasis is placed on the overall prediction skill and the dependence of the skill on MJO amplitude and phase.

a. Overall MJO prediction skill

Figure 2 shows the bivariate ACC and RMSE of MJO prediction during boreal winter. The ACC curve for individual members (gray lines in Fig. 2a) drops gradually during the first 10 days (ACC > 0.78) and then drops rapidly on the subsequent 10–50 days. The single-member mean skill is about 22 days with the criterion of ACC exceeding 0.5. As expected, the ACC for the six-member ensemble mean (red line in Fig. 2a) is superior to that from individual members, in particular for lead time beyond 15 days, and the ACC curve shows a very linear character, with the skill reaching out to 27 days (also Table 1). Utilization of the six-member ensemble mean has increased the skill by about 5 days compared to the single-member skill. Meanwhile, the RMSE exhibits rapid growth during the first 15 days followed by a period of slower error growth (Fig. 2b). The effect of the ensemble mean becomes prominent after around 15 days, supported by the strong contrast between individual members and the ensemble mean for both ACC and RMSE. Note that only the six-member ensemble mean results are presented hereinafter.

Using the same criterion of ACC in excess of 0.5, the prediction skills for RMM1 and RMM2 are estimated to be 29 and 24 days (not shown), respectively, suggesting that the EOF1 is more predictable than the EOF2 mode in this model forecast system. This may be linked to the model's deficiency in simulating EOF2 mode as the EOF2 mode shows relatively larger bias with respect to its spatial pattern than EOF1 as shown in Fig. 1. Following Kim et al. (2014), we also investigated the prediction skill for individual variables. As expected, the prediction skill for OLR is lower (22 days) than the other two circulation variables U850 (25 days) and U200 (24 days). One reason is that OLR is tightly linked to convection that is more difficult to predict than circulations.

As mentioned in section 2, the hindcast anomalies are obtained by subtracting the model hindcast climatology that calls for large sample of experiments, so that this methodology may not be applied to the case with a relatively small sample of forecasts. To show the robustness of the results, we use other approaches to isolate MJO from model hindcasts. First, we apply an identical methodology as that used to obtain the observational anomalies. Results show that the ACC curve drops much faster during the first 15 days than the results

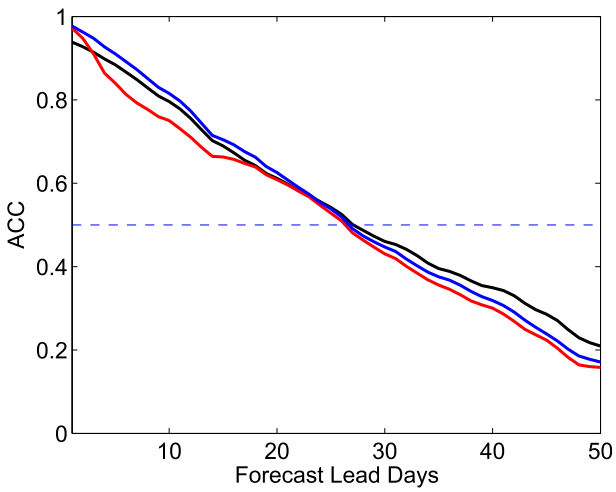

FIG. 3. The bivariate ACC for all cases using different methodologies to obtain anomalous fields for hindcast experiments. The black lines are results removing the model forecast climatology and the previous 120-day mean; the red one is for results removing the time mean and first 3 harmonics from observed annual cycle, and also the previous 120-day mean. The blue line is similar to red one but applying a mean bias correction.

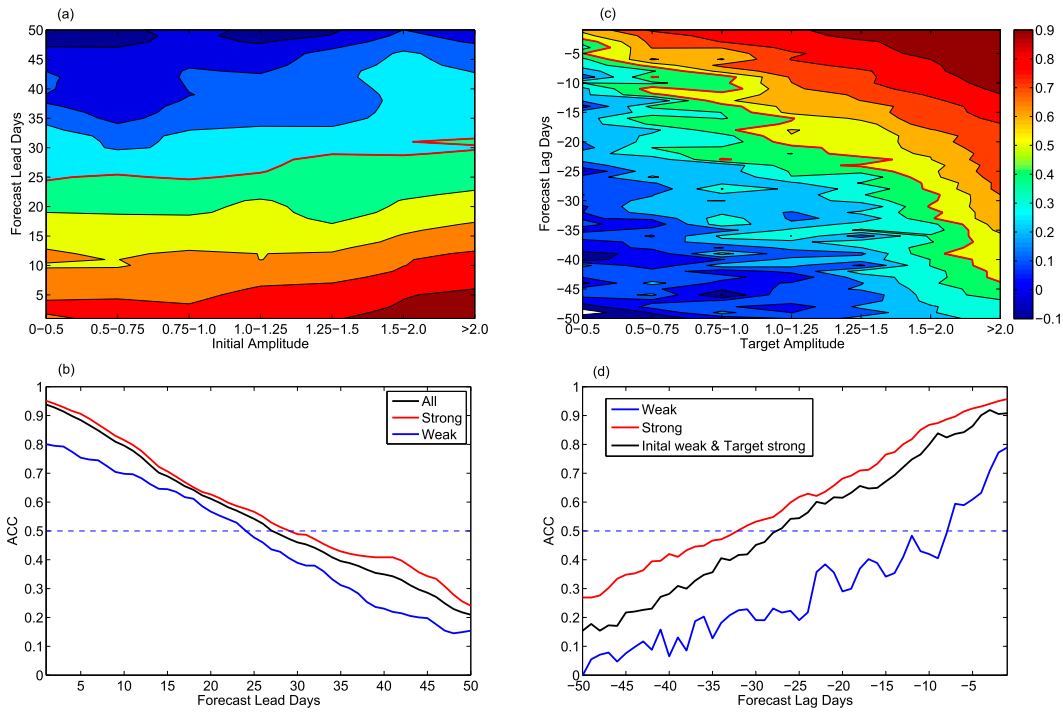

FIG. 4. (a) The bivariate ACC as a function of initial MJO amplitude (x axis) and forecast lead days (y axis). The contour interval is 0.1 and the red contour represents the correlation coefficient of 0.5. (b) The bivariate ACC for all cases (black), initially strong cases (MJO amplitude greater than 1; red), and initially weak cases (MJO amplitude less than 1; blue). (c),(d) As in (a),(b), but for the target MJO amplitude as a function of forecast lag days. The black line in (d) represents the ACC for initial weak but target strong cases.

by removing the hindcast climatology, but the prediction skill still reaches 26 days (Fig. 3). To understand what causes the sudden drop of ACC within 15 days, an additional step is performed: computing the mean of the anomalies (obtained from the first two steps) for all hindcasts (regardless of the calendar) and then subtracting it from each day's anomalous fields for each hindcast experiment. This step can be regarded as a bias correction as the model predictions tend to drift toward the model's mean climate with the increased forecast lead time. The mean bias correction dramatically improves the ACC especially during the first 15 days as the model initial shock and mean state drift are most pronounced at this time period (not shown). The skill reaches 27 days, implying the robustness of our results by using diverse methodologies.

b. *Skill dependence on MJO amplitude*

Many previous studies have demonstrated that the MJO prediction skill depends on the initial amplitude of the MJO, with higher prediction skill for initially strong cases than initially weak cases (Lin et al. 2008; Kang and Kim 2010; Rashid et al. 2011; Wang et al. 2014; Kim et al. 2014). Our results show that the ACC displays a modest increase along with the enhancement of the initial amplitude (Fig. 4a). The initially strong cases show a systematically higher ACC than the initially weak cases from the first day of forecast, while the ACC decrease is relatively slower for initially weak cases during the first 18 days (Fig. 4b). The initially strong (weak) cases have skill of 29 (24) days (Fig. 4b and Table 1). We speculate that the relatively lower prediction skill for initially weak cases is partly ascribable to the lack of signal in the initial condition.

The above results imply that the model has high prediction skill starting from an existing MJO. By contrast, prediction of the MJO genesis tends to be more challenging but may be more meaningful to represent the model's capability in MJO prediction. Figure 4c shows the ACC as a function of target amplitude and forecast lag days. Note that here the cases include both the initially strong and weak cases. Here the day 0 represents the occurrence time for the target MJO events and the negative number is the lag days before the MJO occurrence. When the target MJO amplitude is less than 0.5, the model almost has no skill. A higher skill is achieved along with the enhancement of the target amplitude. The skill reaches about 17 days when the target amplitude is between 0.75 and 1.5, and the skill dramatically jumps to more than 34 days when the target amplitude larger than 1.5. On average, the target strong (amplitude larger than 1) cases have skill of 32 days while the target weak (amplitude less

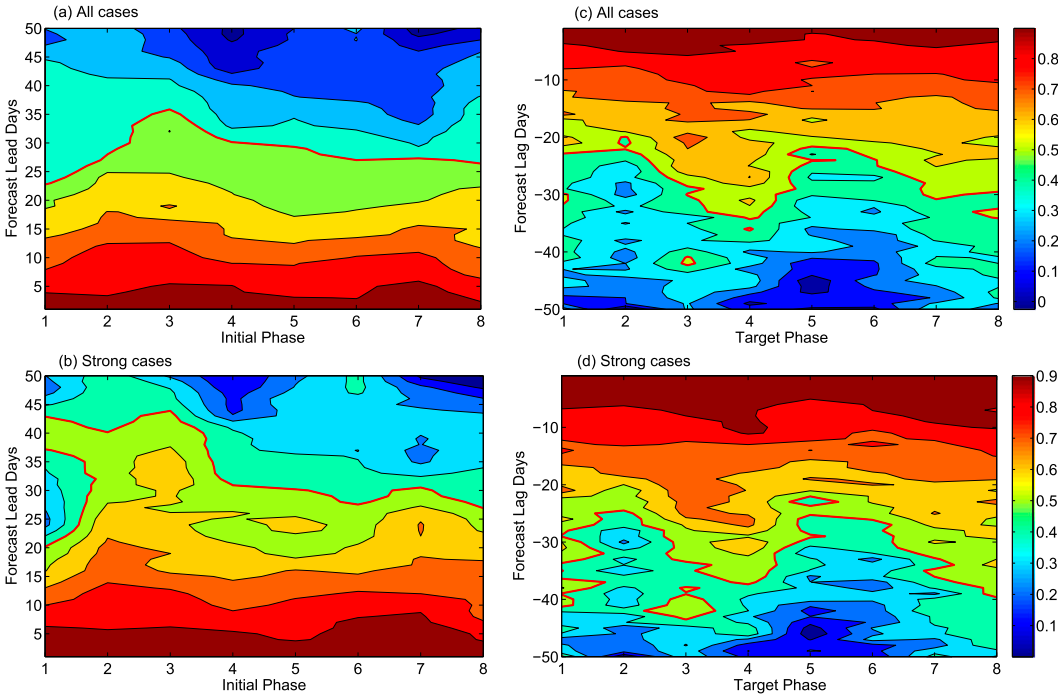

FIG. 5. The bivariate ACC as a function of different initial phases (x axis) and forecast lead days (y axis) for (a) all cases and (b) initially strong cases. (c),(d) As in (a),(b), but for the skill as a function of target phase (x axis) and forecast lag days (y axis). The contour interval is 0.1 and the red contours represent the correlation coefficient of 0.5.

than 1) cases only have skill of 7 days (Fig. 4d and Table 1). Compared with the target strong cases, the poorer skill for target weak cases is attributed to the smaller ACC at forecast lag day −1 and also the more rapid decrease of ACC during the first 15 days. The onset or initiation prediction for primary MJO events may be roughly estimated by exploring the prediction skill for initially weak but target strong cases, and the skill reaches 27 days (Fig. 4d).

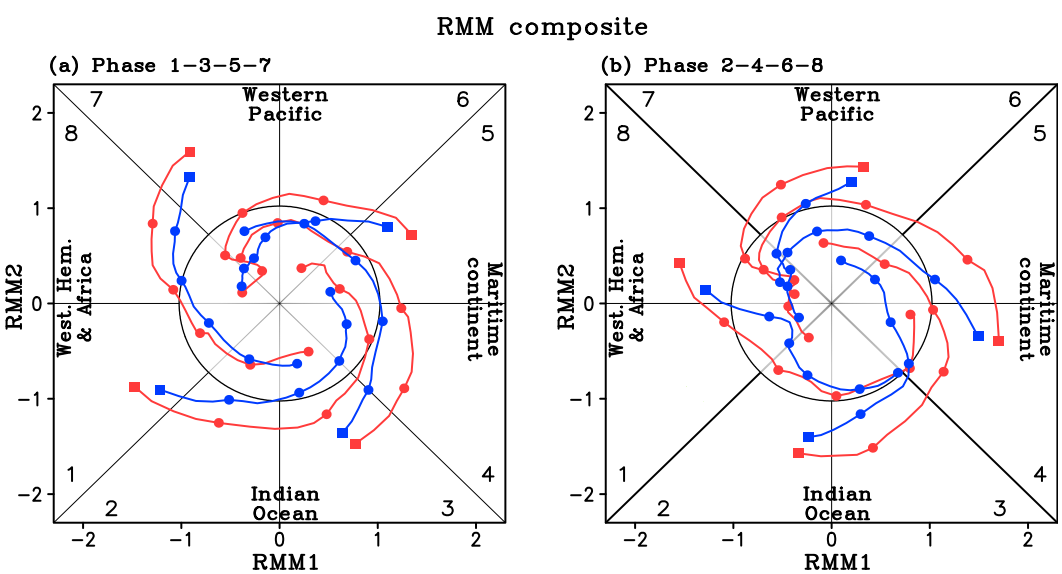

FIG. 6. The RMM composite phase–space diagram for the first 25 days from observations (red) and the model predictions (blue) initialized at different phases. The results are for the composite of strong cases only. The dots reflect every 5 days from the forecast starting date (day 1; filled squares).

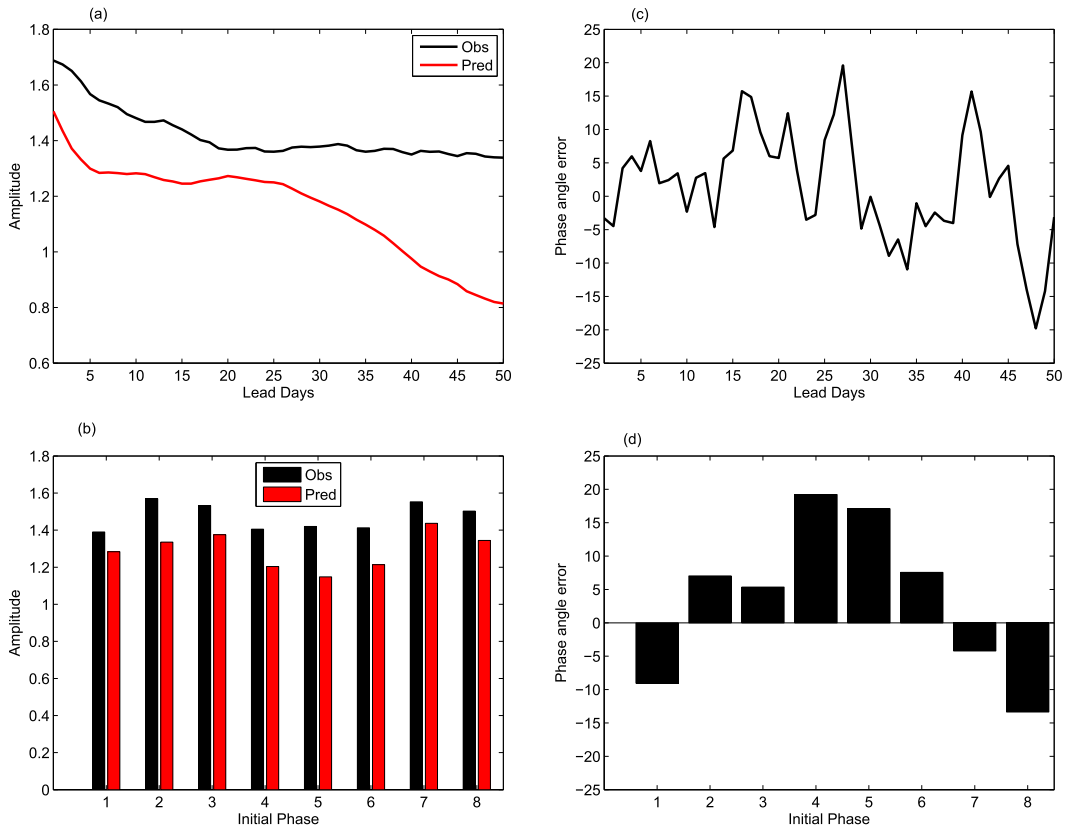

FIG. 7. (a) Evolution of MJO amplitude as a function of lead days for the initially strong cases for observations (black) and model prediction (red). (b) The observed (black bars) and predicted (red bars) MJO amplitude averaged over the first 25 days for the cases initialized at different MJO phases (x axis). (c) Prediction of MJO phase angle error (°) as a function of lead time for the initially strong cases. (d) The predicted MJO phase error averaged over the first 25 days for the cases initialized at different MJO phases (x axis).

c. *Skill dependence on MJO phase*

The MJO prediction skill may also rely on the MJO phase when the forecasts are initialized. Here, each phase has approximately 50 cases and each strong phase has about 30 cases. As shown in Fig. 5a, the skill contrast among different initial phases is relatively small, with phases 3, 4, and 5 above the mean skill and phases 1 and 8 slightly less than the mean. The contrast becomes more prominent for initially strong cases: the skill is beyond 40 days for hindcasts initialized at phases 2 and 3, and about 20–30 days for the other phases (Fig. 5b).

The ACC skill shows its dependence on the target phase and the forecast lag days (Fig. 5c). It is clear that the target phases 3, 4, 7, and 8 have slightly higher skill (about 30 days) than the other four phases (phases 1, 2, 5, and 6; about 21 days). The results are also evident for target strong cases (Fig. 5d). The skill contrast is consistent with the result that RMM1 is more predictable than RMM2, as RMM1 (RMM2) represents a typical convection–circulation pattern for phases 3 and 4 (5 and 6). Note that phases 7 and 8 (1 and 2) are the corresponding negative counterparts for phases 3 and 4 (5 and 6). This can be traced back to the bias in the EOF2 mode that shows a broader wind pattern than observation (Fig. 1d).

Some models exhibited the so-called MC prediction barrier with the predicted MJO signal having difficulty propagating across the MC (Vitart and Molteni 2010; Lin et al. 2008; Fu et al. 2011). This version of the GFDL model achieves higher skill for hindcasts initialized at phases 2 and 3 than the mean prediction skill, indicating that the model may not suffer the MC prediction barrier limitation. In agreement with several previous studies (e.g., Neena et al. 2014; Kim et al. 2014), these results suggest that the MC prediction barrier could be highly model dependent.

4. Evaluation of MJO amplitude and propagation prediction

To depict the characteristics of propagation and amplitude, a phase–space diagram is plotted for comparison between the observed and predicted MJO

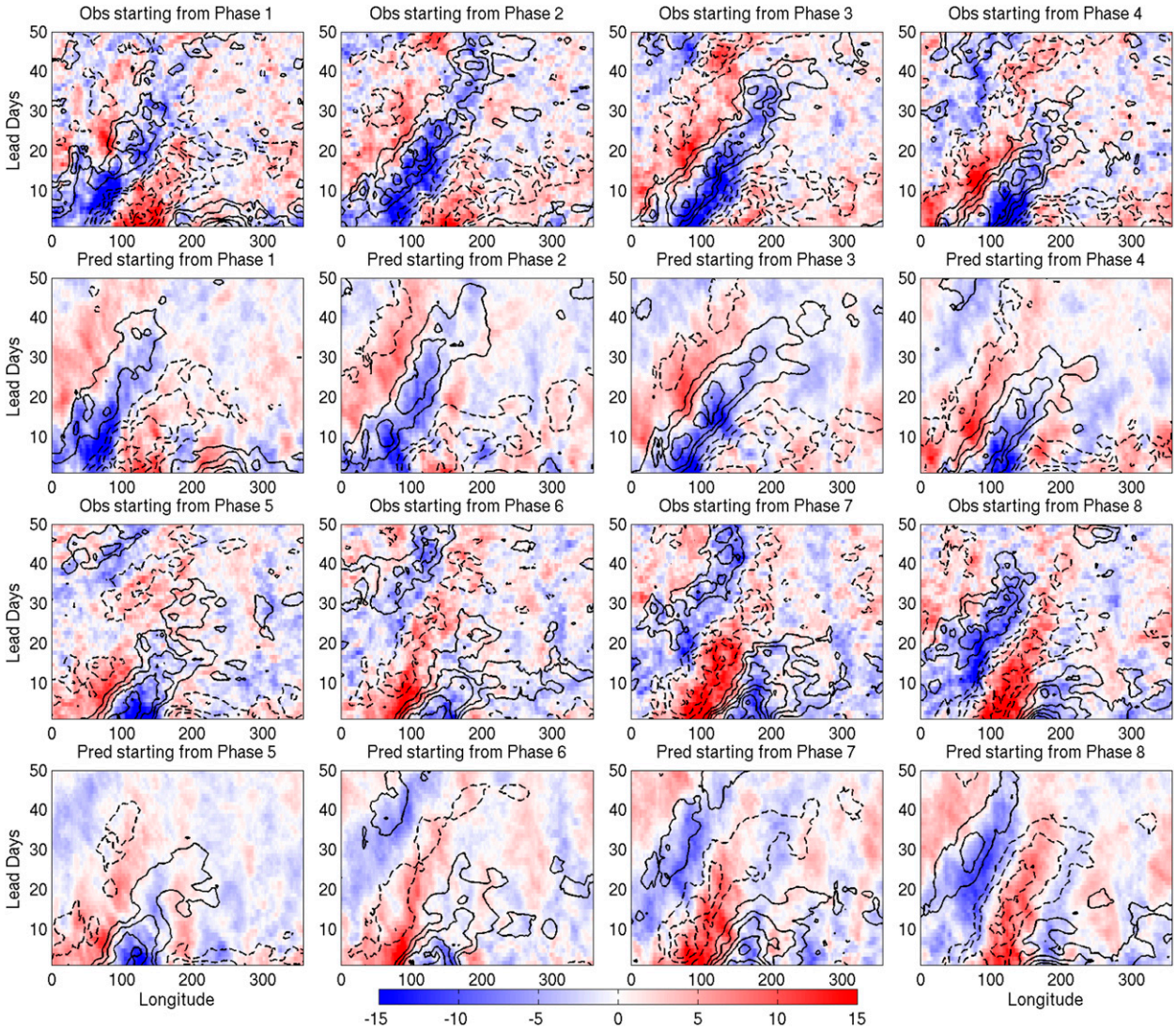

FIG. 8. Composite anomalies of the OLR (shading; $\mathrm{W\,m^{-2}}$) and U850 [contour interval of $0.5\,\mathrm{m\,s^{-1}}$ starting at $+0.5$ (solid) and $-0.5\,\mathrm{m\,s^{-1}}$ (dashed)] averaged over 15°S–15°N initiated at eight different phases. The x axis is for longitude and the y axis is for forecast lead days. The panels in the first and third rows are for observations and in the second and fourth rows are for model predictions. Here the results are based on initially strong MJO events only.

indices with respect to different phases (Fig. 6). This diagram represents the composite results of the time evolution of RMM indices starting with an initially strong MJO. The phase diagram is plotted for a 25-day target period with solid dots representing the phase locations every 5 days. The amplitude is generally decaying with time for both observations and hindcast results. The predicted MJO amplitude is in qualitative agreement but weaker than observations.

The amplitude and propagation are further assessed in Fig. 7. As a common bias for current model forecast systems (e.g., Rashid et al. 2011; Wang et al. 2014; Kim et al. 2014; Neena et al. 2014), the predicted MJO amplitude is underestimated with the mean amplitude underestimated by about 12.5% averaged over the first 25 days. The amplitude error on day 30 is similar to that on day 1, indicating that large portion of amplitude error may be attributed to the initial bias. For individual phase, the underestimated amplitude during the first 25 days is most evident in phases 4, 5, and 6 (Fig. 7b). The phase angle error is used to estimate the propagation speed bias. The mean phase angle error is weakly positive during the first 30 days with a mean value of 4.2° for the first 25 days (Fig. 7c). For the mean of the first 25 days, the phase angle error varies among different phases with negative error for phases 1, 7, and 8 but positive error for the other phases (Fig. 7d).

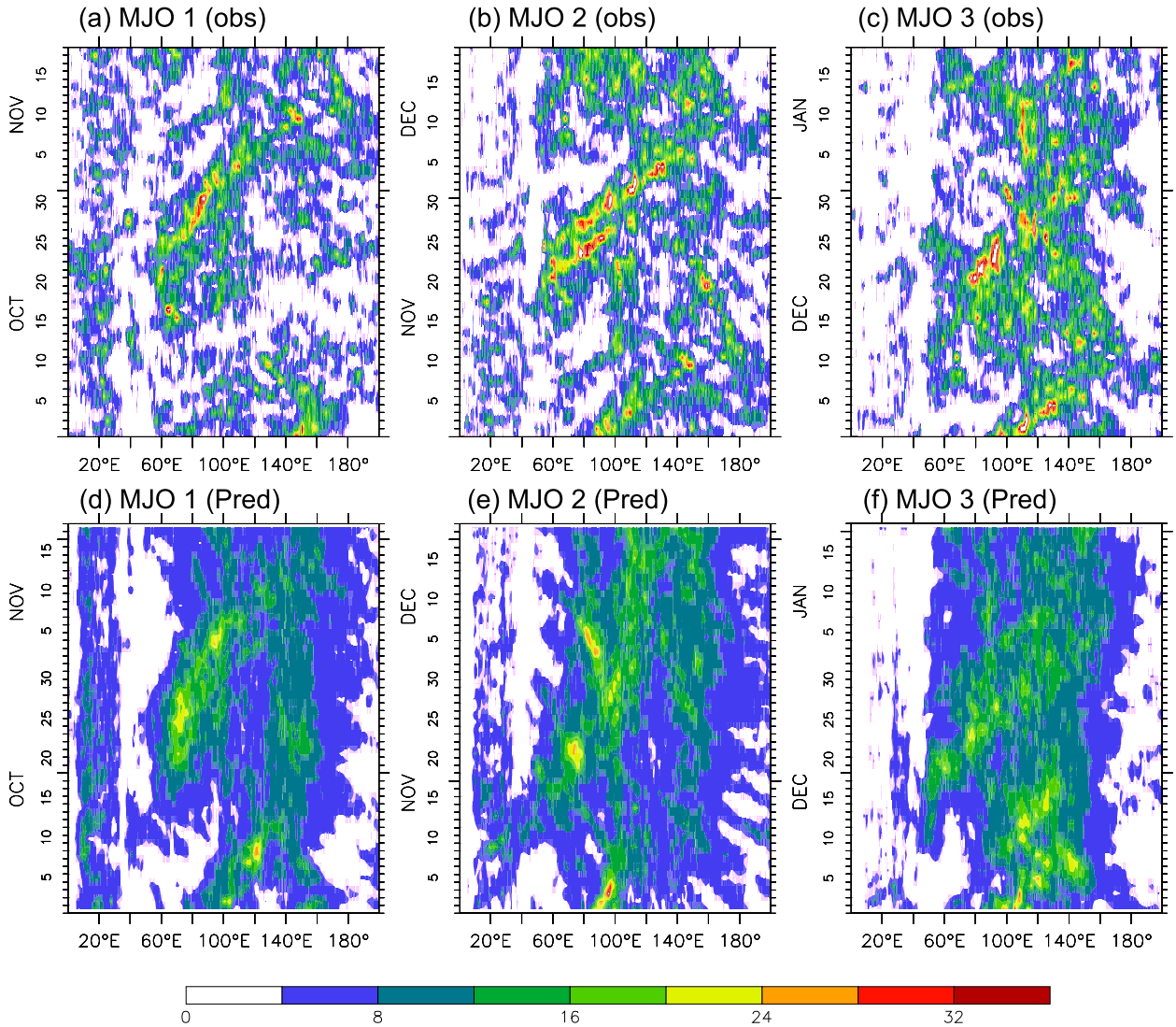

FIG. 9. The longitude–time diagram of the composite anomalies of precipitation (mm day^{-1}) averaged over 10°S–10°N initiated on the first day of each month from October to December 2011, (a)–(c) for observations and (d)–(f) for model predictions.

Figure 8 displays the composite results of OLR and U850 anomalies averaged over 15°S–15°N for initially strong cases. Overall, the model realistically predicts the amplitude and eastward propagation of MJO for each phase as well as the lead–lag relationship between convection and circulation. For phases 3, 4, 7, and 8, an opposite phase of MJO convection anomalies develops over the Indian Ocean after about 20 days, likely triggered by the primary MJO (Matthews 2008). It gives us a clue that this model may have some capability in predicting the occurrence of successive MJOs. After crossing the MC, the predicted MJO propagation speed tends to become faster than that in the Indian Ocean and MC, resulting in a broad peak of wind pattern in the EOF2 mode (Fig. 1d). Another interesting feature is found for the asymmetry of the observed convection–circulation anomalies. For example, starting from phase 2, the wet anomalies accompanied by westerly wind exhibits a strong and well-organized coupled system propagating eastward starting from the Indian Ocean. For the counterpart phase 6, the OLR and U850 are significantly weaker and the eastward propagation is less organized. This asymmetry is also well predicted in the model.

5. MJO prediction during the DYNAMO/CINDY period

In this section, special attention is put on the DYNAMO/CINDY field campaign period (September 2011–March

2012) with large amounts of in situ observations (Yoneyama et al. 2013; Zhang et al. 2013; Sobel et al. 2014; Wang et al. 2015). Given the relatively small forecast sample, the anomalous fields are calculated by removing the time mean, the first 3 harmonics of the observational annual cycle, and the mean of all hindcast anomalies during this period. During these seven months, this model shows a prediction skill of 29 days for all cases and 33 days for initially strong cases (not shown). The skill is slightly higher than the mean skill during boreal winter, which is likely due to more occurrences of MJO events (5) during this period than average (3–4 events). The results are encouraging when compared to other model results: Fu et al. (2013) showed that CFSv2 model and University of Hawaii coupled model have prediction skill of 25 and 28 days, respectively, during the same DYNAMO/CINDY period. We also show three MJO events from mid-October to December 2011 (Fig. 9). The prediction starts the first day of October, November, and December 2011 with an initial phase of 6, 4, and 4, respectively. In general, the model accurately predicts the subsequent eastward propagation of the precipitation signal from the MC to the central Pacific. The geneses of three major MJO events are also well predicted with a lead time of about half a month in spite of the underestimated precipitation magnitude. The eastward propagation speed tends to be slower than observations for the first (MJO 1) and second MJO (MJO 2) and the simulated propagation of the MJO event (MJO 3) is faster (and closer to the observations) than MJO 1 and MJO 2. The precipitation is notably widespread in the model.

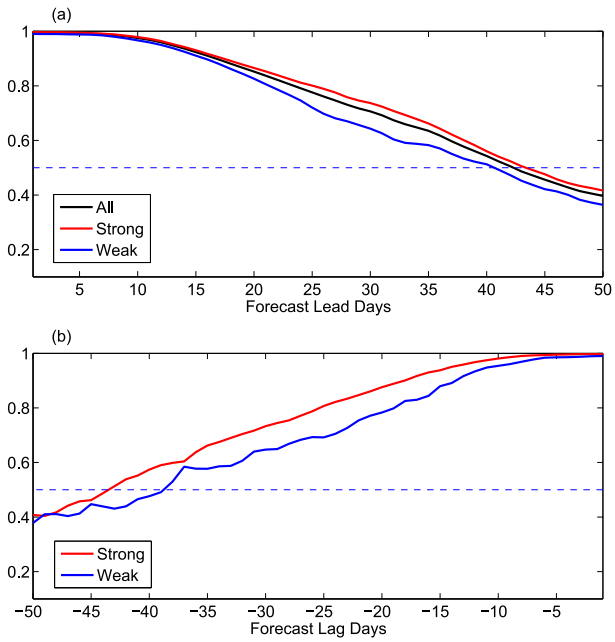

FIG. 10. (a) Potential predictability for all cases (black), initially strong cases (red), and initially weak cases (blue) as a function of forecast lead days. (b) Potential predictability for target strong (red) and target weak (blue) cases as a function of forecast lag days.

6. Summary and discussion

a. Summary

The importance of accurate MJO forecasts has been emphasized as it is a critical component for extended-range forecasts (2–4 weeks) (e.g., Waliser 2006). The GFDL model has been widely used in climate study whereas the MJO prediction skill has not been evaluated. This study aims to examine the MJO prediction skill during boreal winter for a new version of the GFDL coupled model. With a simple nudging technique for both atmospheric variables and SST, it is demonstrated that the model possesses a prediction skill out to 27 days by examining 11 years of hindcast experiments from 2003 to 2013 (Table 1). Results also show that the initially (and target) strong MJO cases achieve higher prediction skill than the initially (and target) weak cases. The propagation speed is well predicted in the model, which is largely responsible for the high ACC during the time range of 20–40 days. The MJO prediction skill also shows some sensitivity with respect to the initial and target phases which may provide useful information for real-time prediction. The MJO prediction over the DYNAMO/CINDY period is also assessed and the skill reaches out to 29 days (Table 1). The results are encouraging especially considering that no data assimilation is adopted in this forecast system.

b. Discussion

The model's potential predictability measures the upper bound of the MJO prediction skill, and can be used to quantify the gap between the prediction skill and predictability. Neena et al. (2014) found that the MJO predictability estimated by the signal-to-noise ratio using ensemble-mean hindcasts was around 35–45 days for most current models. Here we use a different approach following Rashid et al. (2011) by taking one of the six members as the "truth" and the skill of the ensemble mean computed from the other five members is scored against it. The six time series of bivariate ACC can be achieved by selecting each member as the truth. Here strong assumptions are used that both the model and initial conditions are perfect. Results suggest that the potential predictability is 42 days for this model (Fig. 10a and Table 1), indicating that this model has the scope for further improving its MJO prediction skills by up to 15 days before reaching the upper limit of potential

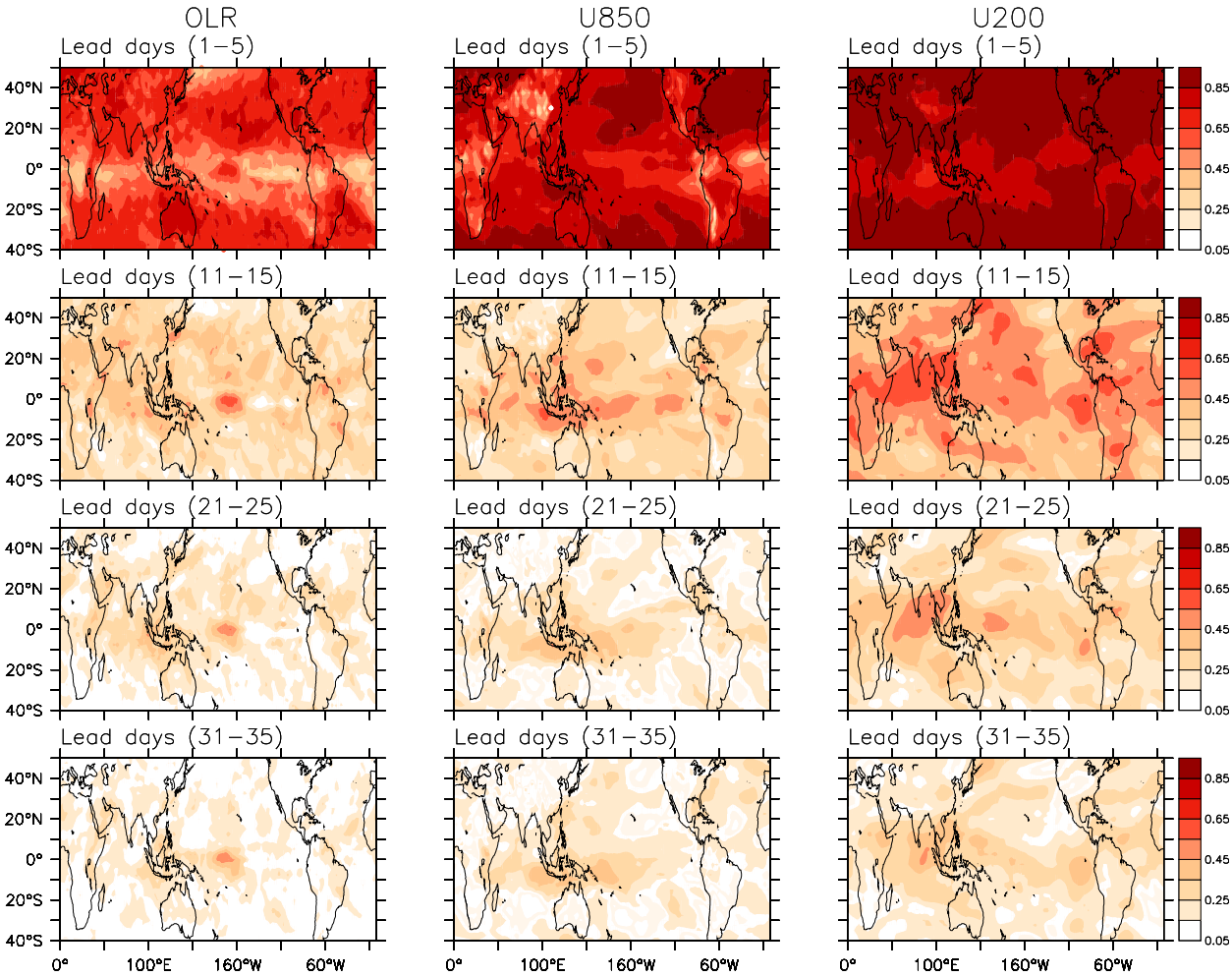

FIG. 11. The spatial correlation coefficient between observed and predicted 5-day mean (left) OLR, (center) U850, and (right) U200 anomalies for lead times (top)–(bottom) of 1–5, 11–15, 21–25, and 31–35 days for all cases (only the values above 0.15 are shown at 95% significance level).

predictability. The predictability for individual phase is also studied and results show that the predictability is all beyond 40 days (not shown). Meanwhile, the predictability is about 43 and 40 days for initially strong and weak cases, and 43 and 38 days for target strong and weak cases, respectively (Fig. 10). This implies that the target weak cases have the largest gap between the real prediction skill and potential predictability (31 days).

One simple way to improve the current skill is to enhance the ensemble spread. The model's prediction skill largely relies on the spread for the ensemble members, which can be estimated by the standard deviation of ensemble members relative to the ensemble mean (Kim et al. 2014). A perfect model forecast system requires that the ensemble spread equals to the error of the ensemble mean (Weisheimer et al. 2011; Kim et al. 2014). Similar to the NCEP CFSv2 and ECMWF VarEPS models (Kim et al. 2014), the current model prediction system also bears the same problem with underdispersive ensemble members (Fig. 2b). In particular, the model spread is only about 0.1 during the first 5 days, which is 5 times less than the corresponding RMSE. This problem is partly related to the simple initialization method we adopted. Thus, a simple way to improve the current model prediction is to increase the ensemble spread.

The MJO signal has spatial distribution with its maximum over the Indian Ocean–western Pacific sector. To show how the RMM index prediction is reflected on the real prediction, we present the spatial maps of the correlation between the observed and predicted 5-day mean anomalies for all cases using the six-member ensemble mean results (Fig. 11). Note that the anomalous fields include not only MJO but also all other intraseasonal variability. For lead times of 1–5 days, the maximum correlation skill for all these three anomalous fields appears over the subtropics for both land and ocean. Relatively lower skill over the tropical ocean

area is arguably linked to the unrealistic prediction of convection and clouds over the tropics in the model. Comparing with OLR prediction, the circulation prediction (U850 and U200) shows a superior prediction skill. As time goes on, the skill over the subtropics decreases rapidly as the intraseasonal predictability source (MJO) is mainly residing over the tropics, particularly over the Indian Ocean–western Pacific sector. It is interesting to see that the U850 and OLR prediction is effective for lead time of 31–35 days over the western-to-central Pacific, which may facilitate the ENSO prediction. Different from the other two fields, U200 has the best prediction skill over the northern Indian Ocean. Some skill is also found over the midlatitude for both U200 and U850, particularly over the Atlantic Ocean, which is arguably linked to the MJO's remote forcing effect on the NAO (Cassou 2008).

In this study, we are only focusing on the boreal winter season. One important reason is that the RMM indices may not be sufficient in describing the boreal summer MJO activities, in particular the northward propagation component (Lee et al. 2013). A further study is planned to explore the prediction skill in boreal summer by employing the indices proposed by Lee et al. (2013) to assess the boreal summer MJO.

Acknowledgments. We appreciate the help from Hye-Mi Kim and J. M. Neena. The authors also benefitted from the discussion with Isaac Held. The authors gratefully acknowledge support from the NOAA MAPP Program under Awards NA12OAR4310075, China National 973 project 2015CB453200 (TL), and Climate Program Office, Climate Variability and Predictability Program (GC14-252).

REFERENCES

Alaka, G. J., and E. D. Maloney, 2012: The influence of the MJO on upstream precursors to African easterly waves. *J. Climate,* **25,** 3219–3236, doi:10.1175/JCLI-D-11-00232.1.

Benedict, J. J., and D. A. Randall, 2007: Observed characteristics of the MJO relative to maximum rainfall. *J. Atmos. Sci.,* **64,** 2332–2354, doi:10.1175/JAS3968.1.

——, E. D. Maloney, A. H. Sobel, D. M. Frierson, and L. J. Donner, 2013: Tropical intraseasonal variability in version 3 of the GFDL Atmosphere Model. *J. Climate,* **26,** 426–449, doi:10.1175/JCLI-D-12-00103.1.

Brunet, G., and Coauthors, 2010: Collaboration of the weather and climate communities to advance subseasonal-to-seasonal prediction. *Bull. Amer. Meteor. Soc.,* **91,** 1397–1406, doi:10.1175/2010BAMS3013.1.

Camargo, S. J., M. C. Wheeler, and A. H. Sobel, 2009: Diagnosis of the MJO modulation of tropical cyclogenesis using an empirical index. *J. Atmos. Sci.,* **66,** 3061–3074, doi:10.1175/2009JAS3101.1.

Cassou, C., 2008: Intraseasonal interaction between the Madden–Julian oscillation and the North Atlantic Oscillation. *Nature,* **455,** 523–527, doi:10.1038/nature07286.

Donald, A., H. Meinke, B. Power, M. C. Wheeler, A. Maia, N. White, R. C. Stone, and J. Ribbe, 2006: Near-global impact of the Madden–Julian oscillation on rainfall. *Geophys. Res. Lett.,* **33,** L09704, doi:10.1029/2005GL025155.

Fu, X., and B. Wang, 2009: Critical roles of the stratiform rainfall in sustaining the Madden–Julian oscillation: GCM experiments. *J. Climate,* **22,** 3939–3959, doi:10.1175/2009JCLI2610.1.

——, ——, J.-Y. Lee, W. Wang, and L. Gao, 2011: Sensitivity of dynamical intraseasonal prediction skills to different initial conditions. *Mon. Wea. Rev.,* **139,** 2572–2592, doi:10.1175/2011MWR3584.1.

——, J.-Y. Lee, P.-C. Hsu, H. Taniguchi, B. Wang, W. Wang, and S. Weaver, 2013: Multi-model MJO forecasting during DYNAMO/CINDY period. *Climate Dyn.,* **41,** 1067–1081, doi:10.1007/s00382-013-1859-9.

Hsu, P.-C., and T. Li, 2012: Role of the boundary layer moisture asymmetry in causing the eastward propagation of the Madden–Julian oscillation. *J. Climate,* **25,** 4914–4931, doi:10.1175/JCLI-D-11-00310.1.

Hung, M.-P., J.-L. Lin, W. Wang, D. Kim, T. Shinoda, and S. J. Weaver, 2013: MJO and convectively coupled equatorial waves simulated by CMIP5 climate models. *J. Climate,* **26,** 6185–6214, doi:10.1175/JCLI-D-12-00541.1.

Jiang, X., D. E. Waliser, M. C. Wheeler, C. Jones, M.-I. Lee, and S. D. Schubert, 2008: Assessing the skill of an all-season statistical forecast model for the Madden–Julian oscillation. *Mon. Wea. Rev.,* **136,** 1940–1956, doi:10.1175/2007MWR2305.1.

——, M. Zhao, and D. E. Waliser, 2012: Modulation of tropical cyclones over the eastern Pacific by the intraseasonal variability simulated in an AGCM. *J. Climate,* **25,** 6524–6538, doi:10.1175/JCLI-D-11-00531.1.

——, and Coauthors, 2015: Vertical structure and diabatic processes of the Madden–Julian oscillation: Exploring key model physics in climate simulations. *J. Geophys. Res. Atmos.,* doi:10.1002/2014JD022375, in press.

Kang, I.-S., and H.-M. Kim, 2010: Assessment of MJO predictability for boreal winter with various statistical and dynamical models. *J. Climate,* **23,** 2368–2378, doi:10.1175/2010JCLI3288.1.

Kemball-Cook, S. R., and B. C. Weare, 2001: The onset of convection in the Madden–Julian oscillation. *J. Climate,* **14,** 780–793, doi:10.1175/1520-0442(2001)014<0780:TOOCIT>2.0.CO;2.

Kessler, W. S., and R. Kleeman, 2000: Rectification of the Madden–Julian oscillation into the ENSO cycle. *J. Climate,* **13,** 3560–3575, doi:10.1175/1520-0442(2000)013<3560:ROTMJO>2.0.CO;2.

Kim, D., and Coauthors, 2009: Application of MJO simulation diagnostics to climate models. *J. Climate,* **22,** 6413–6436, doi:10.1175/2009JCLI3063.1.

Kim, H.-M., P. J. Webster, V. E. Toma, and D. Kim, 2014: Predictability and prediction skill of the MJO in two operational forecasting systems. *J. Climate,* **27,** 5364–5378, doi:10.1175/JCLI-D-13-00480.1.

Kug, J.-S., F.-F. Jin, K. P. Sooraj, and I.-S. Kang, 2008: State-dependent atmospheric noise associated with ENSO. *Geophys. Res. Lett.,* **35,** L05701, doi:10.1029/2007GL032017.

Lau, W. K.-M., 2005: El Niño Southern Oscillation connection. *Intraseasonal Variability in the Atmosphere–Ocean Climate System,* 1st ed., W. K.-M. Lau and D. E. Waliser, Eds., Springer, 271–305.

Lee, J.-Y., B. Wang, M. C. Wheeler, X. Fu, D. E. Waliser, and I.-S. Kang, 2013: Real-time multivariate indices for the boreal summer

intraseasonal oscillation over the Asian summer monsoon region. *Climate Dyn.,* **40,** 493–509, doi:10.1007/s00382-012-1544-4.

Li, C. Y., X. L. Jia, J. Ling, W. Zhou, and C. D. Zhang, 2009: Sensitivity of MJO simulations to diabatic heating profiles. *Climate Dyn.,* **32,** 167–187, doi:10.1007/s00382-008-0455-x.

Liebmann, B., and C. A. Smith, 1996: Description of a complete (interpolated) outgoing longwave radiation dataset. *Bull. Amer. Meteor. Soc.,* **77,** 1275–1277.

Lin, H., G. Brunet, and J. Derome, 2008: Forecast skill of the Madden–Julian oscillation in two Canadian atmospheric models. *Mon. Wea. Rev.,* **136,** 4130–4149, doi:10.1175/2008MWR2459.1.

Lin, J.-L., and Coauthors, 2006: Tropical intraseasonal variability in 14 IPCC AR4 climate models. Part I: Convective signals. *J. Climate,* **19,** 2665–2690, doi:10.1175/JCLI3735.1.

Lo, F., and H. H. Hendon, 2000: Empirical prediction of the Madden–Julian oscillation. *Mon. Wea. Rev.,* **128,** 2528–2543, doi:10.1175/1520-0493(2000)128<2528:EERPOT>2.0.CO;2.

Madden, R. A., and P. R. Julian, 1971: Detection of a 40–50 day oscillation in the zonal wind in the tropical Pacific. *J. Atmos. Sci.,* **28,** 702–708, doi:10.1175/1520-0469(1971)028<0702:DOADOI>2.0.CO;2.

——, and ——, 1972: Description of global-scale circulation cells in the tropics with a 40–50 day period. *J. Atmos. Sci.,* **29,** 1109–1123, doi:10.1175/1520-0469(1972)029<1109:DOGSCC>2.0.CO;2.

Maloney, E. D., and D. L. Hartmann, 2000: Modulation of hurricane activity in the Gulf of Mexico by the Madden–Julian oscillation. *Science,* **287,** 2002–2004, doi:10.1126/science.287.5460.2002.

Matthews, A. J., 2004: Intraseasonal variability over tropical Africa during northern summer. *J. Climate,* **17,** 2427–2440, doi:10.1175/1520-0442(2004)017<2427:IVOTAD>2.0.CO;2.

——, 2008: Primary and successive events in the Madden–Julian Oscillation. *Quart. J. Roy. Meteor. Soc.,* **134,** 439–453, doi:10.1002/qj.224.

Mo, K. C., 2000: The association between intraseasonal oscillations and tropical storms in the Atlantic basin. *Mon. Wea. Rev.,* **128,** 4097–4107, doi:10.1175/1520-0493(2000)129<4097:TABIOA>2.0.CO;2.

Moon, J.-Y., B. Wang, K.-J. Ha, and J.-Y. Lee, 2013: Teleconnections associated with Northern Hemisphere summer monsoon intraseasonal oscillation. *Climate Dyn.,* **40,** 2761–2774, doi:10.1007/s00382-012-1394-0.

Neena, J. M., J.-Y. Lee, D. Waliser, B. Wang, and X. Jiang, 2014: Predictability of the Madden–Julian oscillation in the Intraseasonal Variability Hindcast Experiment (ISVHE). *J. Climate,* **27,** 4531–4543, doi:10.1175/JCLI-D-13-00624.1.

Rashid, H. A., H. H. Hendon, M. C. Wheeler, and O. Alves, 2011: Prediction of the Madden–Julian oscillation with the POAMA dynamical prediction system. *Climate Dyn.,* **36,** 649–661, doi:10.1007/s00382-010-0754-x.

Reynolds, R. W., T. M. Smith, C. Liu, D. B. Chelton, K. S. Casey, and M. G. Schlax, 2007: Daily high-resolution-blended analyses for sea surface temperature. *J. Climate,* **20,** 5473–5496, doi:10.1175/2007JCLI1824.1.

Rydbeck, A. V., E. D. Maloney, S.-P. Xie, J. Hafner, and J. Shaman, 2013: Remote forcing versus local feedback of east Pacific intraseasonal variability during boreal summer. *J. Climate,* **26,** 3575–3596, doi:10.1175/JCLI-D-12-00499.1.

Seo, K.-H., and W. Wang, 2010: The Madden–Julian oscillation simulated in the NCEP Climate Forecast System model: The importance of stratiform heating. *J. Climate,* **23,** 4770–4793, doi:10.1175/2010JCLI2983.1.

Sobel, A., and E. Maloney, 2012: An idealized semi-empirical framework for modeling the Madden–Julian oscillation. *J. Atmos. Sci.,* **69,** 1691–1705, doi:10.1175/JAS-D-11-0118.1.

——, S. Wang, and D. Kim, 2014: Moist static energy budget of the MJO during DYNAMO. *J. Atmos. Sci.,* **71,** 4276–4291, doi:10.1175/JAS-D-14-0052.1.

Vecchi, G. A., and Coauthors, 2014: On the seasonal forecasting of regional tropical cyclone activity. *J. Climate,* **27,** 7994–8016, doi:10.1175/JCLI-D-14-00158.1.

Vitart, F., 2009: Impact of the Madden Julian Oscillation on tropical storms and risk of landfall in the ECMWF forecast system. *Geophys. Res. Lett.,* **36,** L15802, doi:10.1029/2009GL039089.

——, and F. Molteni, 2010: Simulation of the Madden–Julian oscillation and its teleconnections in the ECMWF forecast system. *Quart. J. Roy. Meteor. Soc.,* **136,** 842–855, doi:10.1002/qj.623.

——, A. W. Robertson, and D. L. T. Anderson, 2012: Subseasonal to seasonal prediction project: Bridging the gap between weather and climate. *WMO Bull.,* **61,** 23–28.

Waliser, D. E., 2005: Predictability and forecasting. *Intraseasonal Variability in the Atmosphere–Ocean Climate System,* 1st ed., W. K.-M. Lau and D. E. Waliser, Eds., Springer, 389–423.

——, 2006: Predictability of tropical intraseasonal variability. *Predictability of Weather and Climate,* 1st ed., T. Palmer and R. Hagedorn, Eds., Cambridge University Press, 275–305.

Wang, B., and T. Li, 1994: Convective interaction with boundary-layer dynamics in the development of a tropical intraseasonal system. *J. Atmos. Sci.,* **51,** 1386–1400, doi:10.1175/1520-0469(1994)051<1386:CIWBLD>2.0.CO;2.

Wang, S., A. H. Sobel, F. Zhang, Y. Q. Sun, Y. Yue, and L. Zhou, 2015: Regional simulation of the October and November MJO events observed during the CINDY/DYNAMO field campaign at gray zone resolution. *J. Climate,* **28,** 2097–2119, doi:10.1175/JCLI-D-14-00294.1.

Wang, W., M.-P. Hung, S. J. Weaver, A. Kumar, and X. Fu, 2014: MJO prediction in the NCEP Climate Forecast System version 2. *Climate Dyn.,* **42,** 2509–2520, doi:10.1007/s00382-013-1806-9.

Weisheimer, A., T. N. Palmer, and F. J. Doblas-Reyes, 2011: Assessment of representations of model uncertainty in monthly and seasonal forecast ensembles. *Geophys. Res. Lett.,* **38,** L16703, doi:10.1029/2011GL048123.

Wheeler, M. C., and H. H. Hendon, 2004: An all-season real-time multivariate MJO index: Development of an index for monitoring and prediction. *Mon. Wea. Rev.,* **132,** 1917–1932, doi:10.1175/1520-0493(2004)132<1917:AARMMI>2.0.CO;2.

Xiang, B., and Coauthors, 2014: Beyond weather time-scale prediction for Hurricane Sandy and Super Typhoon Haiyan in a global climate model. *Mon. Wea. Rev.,* **143,** 524–535, doi:10.1175/MWR-D-14-00227.1.

Yoneyama, K., C. Zhang, and C. N. Long, 2013: Tracking pulses of the Madden–Julian oscillation. *Bull. Amer. Meteor. Soc.,* **94,** 1871–1891, doi:10.1175/BAMS-D-12-00157.1.

Zhang, C., 2013: Madden–Julian oscillation: Bridging weather and climate. *Bull. Amer. Meteor. Soc.,* **94,** 1849–1870, doi:10.1175/BAMS-D-12-00026.1.

——, and J. Gottschalck, 2002: SST anomalies of ENSO and the Madden–Julian oscillation in the equatorial Pacific. *J. Climate,* **15,** 2429–2445, doi:10.1175/1520-0442(2002)015<2429:SAOEAT>2.0.CO;2.

——, ——, E. D. Maloney, M. W. Moncrieff, F. Vitart, D. E. Waliser, B. Wang, and M. C. Wheeler, 2013: Cracking the MJO nut. *Geophys. Res. Lett.,* **40,** 1223–1230, doi:10.1002/grl.50244.